Precision Engineering 88 (2024) 674–685

Contents lists available at ScienceDirect

Precision Engineering

journal homepage: www.elsevier.com/locate/precision

A novel F-shaped linear guiding mechanism based compliant positioning stage with restricted parasitic motion☆

Yitong Li [a], Tingting Ye [b], Jie Ling [c], Xiaohui Xiao [a], Zhao Feng [a,d,*]

[a] School of Power and Mechanical Engineering, Wuhan University, Wuhan 430072, China
[b] Department of Industrial and Systems Engineering, The Hong Kong Polytechnic University, Kowloon, 999077, Hong Kong SAR, China
[c] College of Mechanical and Electrical Engineering, Nanjing University of Aeronautics and Astronautics, Nanjing 210016, China
[d] Wuhan University Shenzhen Research Institute, Shenzhen 518057, China

ARTICLE INFO

Keywords:
Linear guide
Compliance matrix method
Flexure hinges
Compliant mechanism
Straight-line motion

ABSTRACT

Positioning stages are significant in precision technologies under higher demands of operation and manufacturing. The performance of the selected guiding mechanisms is a decisive factor affecting the positioning accuracy of the stage. To restrict the parasitic motions along the degrees of constraint during motion transmission, a piezo-actuated compliant positioning stage with novel F-shaped linear guiding mechanisms (FLGM) is developed in this paper to enable a precision motion. With a simple and compact structure, a single FLGM can generate an approximate straight-line motion and enhance the transverse stiffness. Four FLGMs are arranged symmetrically in parallel to theoretically eliminate the parasitic motions, bringing in the merits of a low coupling rate and a wide bandwidth in the working direction. A stack piezoelectric actuator embedded in a forward bridge-type displacement amplifier is utilized to drive the guided stage. Analytical modeling of its kinematic, static, and dynamic characteristics is mathematically established by utilizing the pseudo-rigid-body method, compliance matrix method, and Lagrange's equation. Finite element analysis is conducted and a fabricated prototype is experimentally tested, validating the veracity of the analytical models. Experimental results show that the parasitic motion is constrained by the guiding mechanism effectively with a coupling rate below 0.95%, and a high natural frequency of 856.9 Hz is achieved simultaneously.

1. Introduction

Precision positioning stages have been playing a crucial role in precision technologies including operation, measurement, and manufacturing. They have been widely utilized in precision systems relating to the fields of biomedical engineering [1,2], precision fabrication [3], atomic force microscopy [4], robotics [5] and many more. Compliant mechanism (CM) is the primary choice in precision positioning stages as the motion transmission module owing to their distinctive characteristics. CMs can be easily fabricated due to their monolithic and miniaturized structure, with no need for assembly or lubrication, and introduce no wear, backlash, or interstices [6]. In general, functions of CMs can be classified into motion amplification [7,8], motion guidance [9,10], motion decoupling [11–13], constant force/torque adjustment [14–16], and so forth. The main focus of this paper is the innovative conception of an F-shaped compliant linear guiding mechanism for restricting parasitic motions.

Linear guiding mechanisms are indispensable elements for positioning stages. In recent years, the research on guiding mechanisms has attracted continuous interest in the field of CMs. A compliant linear guide can be integrated with amplification mechanisms and actuators to restrict the moving direction along the degrees of freedom (DOFs). They are designed to decrease the inevitable parasitic motions along the degrees of constraint (DOCs) produced by the amplifier, manufacturing error, and misalignment. Their performances are largely determined by the structural configuration. Generally, compliant linear guides can be categorized according to guiding principles into parallelogram type and straight-line motion-generating type.

Among multifarious compliant guiding mechanisms, mechanisms of parallelogram type are the most commonly used for simplicity. The conventional parallelogram mechanism will introduce a vertical parasitic movement which severely reduces the positioning accuracy [17]. Theoretically, the vertical parasitic motion can be counteracted by a symmetrical double parallelogram structure or multistage compound

☆ This paper was recommended by Associate editor Prof. R. Leach.

* Corresponding author at: School of Power and Mechanical Engineering, Wuhan University, Wuhan 430072, China.
E-mail addresses: lyt37729@whu.edu.cn (Y. Li), tilda.ye@connect.polyu.hk (T. Ye), meejling@nuaa.edu.cn (J. Ling), xhxiao@whu.edu.cn (X. Xiao), fengzhao@whu.edu.cn (Z. Feng).

https://doi.org/10.1016/j.precisioneng.2024.04.014
Received 2 January 2024; Received in revised form 15 March 2024; Accepted 17 April 2024
Available online 18 April 2024

parallelogram structure. The former symmetrically connects two parallelograms in parallel to eliminate parasitic motion, while it will increase the stress and decrease the motion range. The latter serially connects several parallelograms to offset the parasitic motions and to enlarge motion ranges, while the natural frequency will be greatly reduced. Nguyen et al. proposed a compliant linear guide embedded symmetrical double parallelogram mechanism to reduce the parasitic motion as well as to enhance the structural rigidity [18]. Zhao et al. developed a dual-stage fast tool servo by serially connecting two different double parallelogram mechanisms actuated by two different piezoelectric actuators (PEAs) to enhance the trajectory tracking performance [19]. Lyu and Xu devised an XY micropositioning stage based on triple-stage compound leaf spring parallelograms, exhibiting a large workspace up to 1.51 cm × 1.48 cm [20]. Gräcer et al. presented a serially arranged compliant stage based on the 10-hinge double parallel mechanism to reduce cross-axis coupling errors and space requirements [21]. Furthermore, the parasitic motions of the conventional parallelogram mechanism can be compensated by replacing the rotational flexure hinges with cross-spring pivots [22].

To obtain better performances, compliant guiding mechanisms of straight-line motion generating type have been proposed gradually. The guided linear movements are generated by various straight-line mechanisms which can produce straight-line paths. Geometric linearity with higher precision can be achieved by adopting straight-line mechanisms. Peaucellier–Lipkin mechanism and Hoeken's linkage are adapted to CMs for generating linear motion [23,24], but they lack compactness. Roberts mechanisms are also utilized to guide straight-line motion. Chen et al. adopted two compliant Roberts mechanisms in a 2-DOF microgripper [25]. Wan et al. introduced a compliant XY micropositioning stage based on the Roberts mechanism with parasitic motion less than 1.7% of the motion stroke but a complex structure and a low natural frequency around 20 Hz [26].

In conclusion, the variety of configurations for compliant linear guiding mechanisms is still insufficient, and there are common issues of inadequate guiding performance, limited motion range, or small bandwidth. Previous studies have revealed the significance of compliant linear guiding mechanisms. Pursuing better mechanical properties of CMs cannot be overemphasized. The main challenges and goals of designing a compliant linear guide are to minimize the parasitic motions, improve the off-axis stiffness ratio, restrain maximum stress, and increase the natural frequencies for better dynamic performance. In an effort to meet the requirements of high-end precision engineering equipment, this paper presents a novel F-shaped linear guiding mechanism based piezo-actuated compliant positioning stage, adopting the straight-line motion generating method to restrict parasitic motion. A novel F-shaped compliant straight-line mechanism with a simple and compact structure is devised and utilized. The proposed linear motion guide has lumped compliance with a novel configuration, which possesses ideal motion linearity, stability, and high bandwidth. A forward bridge-type amplifier (BTA) is embedded to magnify the output displacement of the piezoelectric actuator. The analytical modeling of the kinematics, statics, and dynamics is conducted through the pseudo-rigid-body model (PRBM) method, compliance matrix method (CMM), and Lagrange's equation, respectively. The performances of the compliant stage and the veracity of its analytical modeling will be further verified by finite element analysis (FEA) and experiments.

The remainder of this research is arranged as follows. The configuration design will be first introduced in Section 2. The analytical modeling will be performed in Section 3. Sections 4 and 5 provide the FEA and experimental results and discussions. Finally, the overall conclusions are given in Section 6.

2. Mechanism design

PEA [27], voice coil motor [28] and normal-stressed electromagnetic actuator [29] are the desirable options for driving the CMs on various application scenarios. Among them, PEAs are the most commonly used because of their merits of high stiffness, high natural frequency, sufficient output force, quick response, and the ability to work in environments with strong magnetic fields [27]. Amplification mechanisms are frequently introduced to magnify the PEAs' output displacement because of their weakness of limited stroke. In this paper, a stack piezoelectric ceramic actuator (SPCA) with a forward bridge-type amplification mechanism is adopted for actuating the guiding mechanism based compliant positioning stage.

The computer-aided design model of the proposed compliant positioning stage with linear guiding mechanisms is depicted in Fig. 1. The stage is comprised of a forward BTA embedded with an SPCA and four identical novel F-shaped straight-line guiding mechanisms, with an overall size of 100 mm × 64 mm × 10 mm. The preload screw is involved to generate a pre-tightening force required by the actuator in a simple and effective way. The positioning stage is with lumped compliance at its compliant joints. Basic beam flexure hinges are adopted in the BTA for their small stiffness and double-notch right-circular flexure hinges are adopted in the FLGM for their high motion accuracy [30].

Unfavorable parasitic motion will be inevitably caused in the positioning process because of the intrinsic structural asymmetry and working disturbances. The asymmetry will be caused by the limited machining operation precision and assembling misalignment. To improve the stage's positioning precision, the guided stage is expected to possess a high off-axis stiffness ratio which is defined by the ratio of structural stiffness along the DOCs to the stiffness along the DOF. A single FLGM can generate an approximate straight-line motion at its output end which will be proved in Section 3.1. Therefore, the symmetrical parallel structure is chosen for the guiding modules to guide the linear motion and counteract parasitic motion theoretically.

3. Analytical modeling

3.1. Kinematic modeling

The working principle of the adopted BTA and the proposed FLGM is demonstrated in Fig. 2, which is provided by PRBM method. PRBM is an equivalent rigid-body model of CMs to substitute rotary hinges with torsional springs for the elastic flexures, while other parts are substituted by rigid rods. Once driven with a transverse input displacement generated by the SPCA, the forward BTA will conduct an amplified vertical output displacement along the forward direction which will actuate the positioning stage moving along the DOF of the linear guide. The input and output displacement of the guided stage are represented by u_{in} and y_{out}.

The bridge-type amplifier has been extensively addressed in previous research [31,32]. The kinematic model of the forward BTA is illustrated in Fig. 2(a). The lengths of each pseudo-rigid rod FG and GH and their corresponding rotation angles are denoted by l_1, l_2 and θ_1, θ_2. The kinematic amplification ratio can be derived as:

$$A = \frac{y_{out}}{u_{in}} = \frac{2l_1 \sin\alpha - \sqrt{4{l_1}^2 \sin^2\alpha - {u_{in}}^2 - 4l_1 \cos\alpha u_{in}}}{u_{in}} \tag{1}$$

which will be only decided by the input displacement u_{in} when the design parameters l_1 and α are both determined.

As for the FLGM, the geometric relations can be deduced from Fig. 2(b). A, B, C, D, E are the rotation centers regardless of their subtle draft during deformation. The lengths of each pseudo-rigid rod CD, AB, EB are represented by l_3, l_4, l_5, and their rotation angles are denoted by θ_3, θ_4, θ_5, respectively. In the initial position of FLGM, rod AB is parallel to rod CD, and vertical to rod BE. What is more, hinge C is at the middle point of rod BE. The length of rod BE is equal to the length of rod AB which is half of the length of rod CD. For simplifying the geometric equations, variable parameter a was introduced to calculate

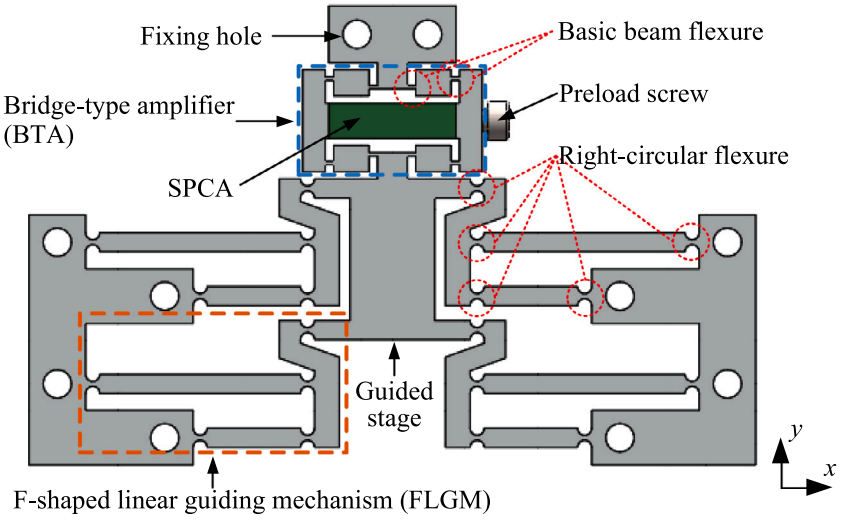

Fig. 1. Schematic diagram of the compliant positioning stage with linear guiding mechanisms.

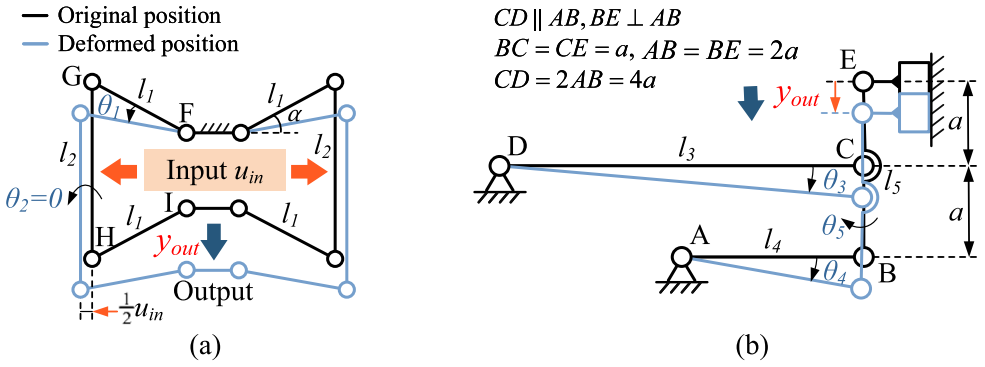

Fig. 2. Pseudo-rigid-body model for kinematic modeling of (a) the forward BTA, (b) a single FLGM.

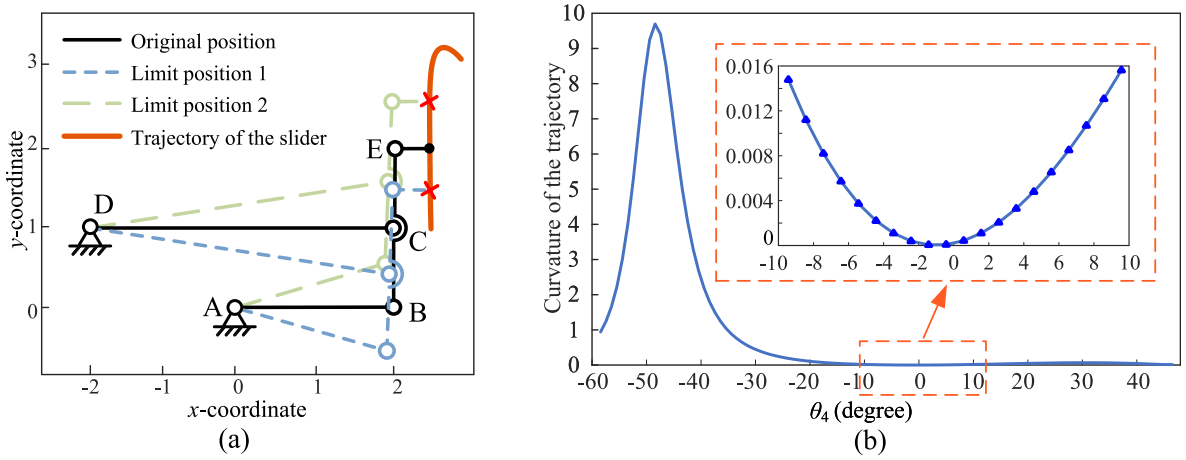

Fig. 3. The approximate straight-line path generated by a single FLGM calculated by kinematic modeling. (a) The positions of the pseudo-rigid bars and the trajectory of the slider, (b) The curvature of the trajectory.

the rods' lengths: $l_3 = 4a, l_4 = 2a, l_5 = 2a$. The following equations can be obtained:

$$\begin{cases} l_4 \sin\theta_4 - \frac{l_5}{2}\cos\theta_5 = l_3 \sin\theta_3 - \frac{l_3}{2} \\ l_4 \cos\theta_4 + \frac{l_5}{2}\sin\theta_5 = l_3 \cos\theta_3 - l_3 + l_4 \\ l_4 \sin\theta_4 - l_5 \cos\theta_5 + l_5 = y_{out}. \end{cases} \tag{2}$$

To measure the straightness of the path of point E, its curvature will be investigated. Establish a coordinate system at point A, then the coordinate of E is:

$$\begin{cases} x_E = l_4 \cdot \cos\theta_4 + l_5 \cdot \sin\theta_5 = \varphi(\theta_4) \\ y_E = l_5 \cdot \cos\theta_5 - l_4 \cdot \sin\theta_4 = \psi(\theta_4). \end{cases} \tag{3}$$

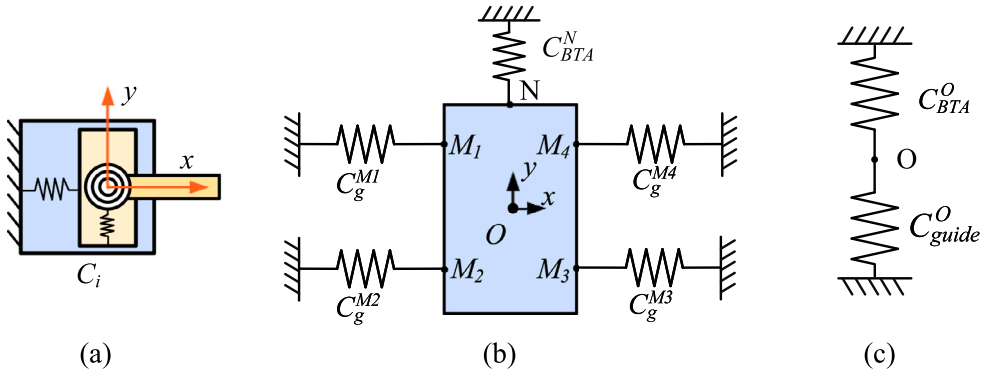

Fig. 4. Equivalent compliance spring model of (a) planar flexure hinges, (b) the guided compliant stage, (c) the BTA and the guiding module at central point O.

Combining (3) with (2) helps eliminating the variable θ_3 and θ_5. Consequently, the curvature of the trajectory of endpoint E can be calculated as a function of the solitary variable θ_4:

$$k = \frac{\varphi'(\theta_4)\psi''(\theta_4) - \psi'(\theta_4)\varphi''(\theta_4)}{\left[\varphi'^2\left(\theta_4\right) + \psi'^2\left(\theta_4\right)\right]^{3/2}} \tag{4}$$

where $\varphi', \varphi'', \psi'$, and ψ'' denote the first and second order derivatives of function $\varphi(\theta_4)$ and $\psi(\theta_4)$ with respect to θ_4.

The kinematic modeling results are presented in Fig. 3. When θ_4 ranges from $-10°$ to $10°$, the curvature k will keep below 0.016 in terms of the kinematic analytical results. It is proved that the guiding module can generate an approximate straight-line motion at its endpoint.

3.2. Static modeling

Static analysis is of great significance to the synthesis of CMs. It reveals the relationship between the input force and the output displacement of the compliant mechanism and will also contribute to the theoretical modeling of the natural frequency. The following calculations are based on the assumption that elastic deformation only occurs at the flexure hinges. Rods between the flexure hinges are deemed as rigid linkages. Since the aforementioned PRBM method only considers the rotary stiffness of flexure hinges, a compliance matrix method [33–35] is employed to establish the static model which considers not only bending moment but also axial force, shear force and their coupled compliance. The compliance matrix method is considered to be an effectual technique for modeling CMs with complex configurations, obviating the need for inner-force analysis. The disadvantages of this method lie in the fact that the input and output stiffness should be modeled separately. It should be clarified that the input stiffness is the force–displacement relation at the input point when the output is blocked, and the output stiffness is the force–displacement relation at the output end when the input port is deemed as rigid.

The adopted matrix method regards planar flexure hinges as three-DOF spring joints which is illustrated in Fig. 4(a). Local coordinate systems are located at the center of the free end of the flexure hinges. The linear displacements at the free end of each flexure hinge along x and y directions are denoted as Δx and Δy. The rotational angle is denoted by $\Delta\theta$. The force and moment acting at the free end are represented by F_x, F_y, and M_z.

The compliance matrix of a flexure hinge is written as:

$$C_i = \begin{bmatrix} c_{11} & 0 & 0 \\ 0 & c_{22} & c_{23} \\ 0 & c_{32} & c_{33} \end{bmatrix} = \begin{bmatrix} \Delta x/F_x & 0 & 0 \\ 0 & \Delta y/F_y & \Delta\theta/F_y \\ 0 & \Delta y/M_z & \Delta\theta/M_z \end{bmatrix} = K_i^{-1} \tag{5}$$

where $c_{23} = c_{32}$, and K_i is the stiffness matrix of the flexure hinge. The in-plane compliance parameters $C_{ij}(i, j = 1, 2, 3)$ are given by the material's elastic modulus and its design parameters in accordance with Castigliano's displacement theorem [36]. Then the displacement–loading relationship at the free end in the local coordinate system of the flexure hinge is:

$$\begin{pmatrix} \Delta x \\ \Delta y \\ \Delta\theta \end{pmatrix} = \begin{bmatrix} c_{11} & 0 & 0 \\ 0 & c_{22} & c_{23} \\ 0 & c_{32} & c_{33} \end{bmatrix} \begin{pmatrix} F_x \\ F_y \\ M_z \end{pmatrix}. \tag{6}$$

With the purpose of acquiring the input and output compliance of the whole compliant mechanism, the compliance matrix C_i at local coordinate system O_i should be transformed into a global coordinate system O_j quantitatively. In light of the homogeneous transformation equation:

$$C_i^j = T_i^j C_i \left(T_i^j\right)^T \tag{7}$$

where the transformation matrix T_i^j is calculated by:

$$T_i^j = R_i^j \cdot P_i^j. \tag{8}$$

The rotation matrices R_i^j with respect to the x, y, and z axes and position matrix P_i^j take on the following forms:

$$R(x,\beta) = \begin{bmatrix} 1 & 0 & 0 \\ 0 & \cos\beta & -\sin\beta \\ 0 & \sin\beta & \cos\beta \end{bmatrix}, R(y,\gamma) = \begin{bmatrix} \cos\gamma & 0 & \sin\gamma \\ 0 & 1 & 0 \\ -\sin\gamma & 0 & \cos\gamma \end{bmatrix}, \\ R(z,\zeta) = \begin{bmatrix} \cos\zeta & -\sin\zeta & 0 \\ \sin\zeta & \cos\zeta & 0 \\ 0 & 0 & 1 \end{bmatrix} \tag{9}$$

$$P_i^j = \begin{bmatrix} 1 & 0 & y_{ji} \\ 0 & 1 & -x_{ji} \\ 0 & 0 & 1 \end{bmatrix} \tag{10}$$

where (x_{ji}, y_{ji}) represents the coordinate of point O_i in the global coordinate system xyO_j, and β, γ, ζ denote the rotation angles counterclockwise from the local coordinate system xyO_i to the global coordinate system xyO_j with respect to axis x, y, or z respectively.

The overall stiffness model of the designed positioning stage is shown in Fig. 4(b) and (c). Point O lies in the center of the central stage. Point N is where the BTA and the stage are connected, and point $M_i(i = 1, 2, 3, 4)$ are where the FLGMs and the stage are connected. To derive the input and output stiffness of the whole guided stage, compliance matrices of each module will be calculated as follows.

As for an FLGM, the local coordinates of each right-circular flexure hinges $xyO_i(i = 1, \ldots, 5)$ and the global coordinate xyM are depicted in Fig. 5. Local compliance matrices of each flexure hinge are expressed by $C_{Oi}(i = 1, \ldots, 5)$. Then their global compliance matrices can be derived by (7):

$$C_{Oi}^M = T_{Oi}^M C_{Oi} \left(T_{Oi}^M\right)^T. \tag{11}$$

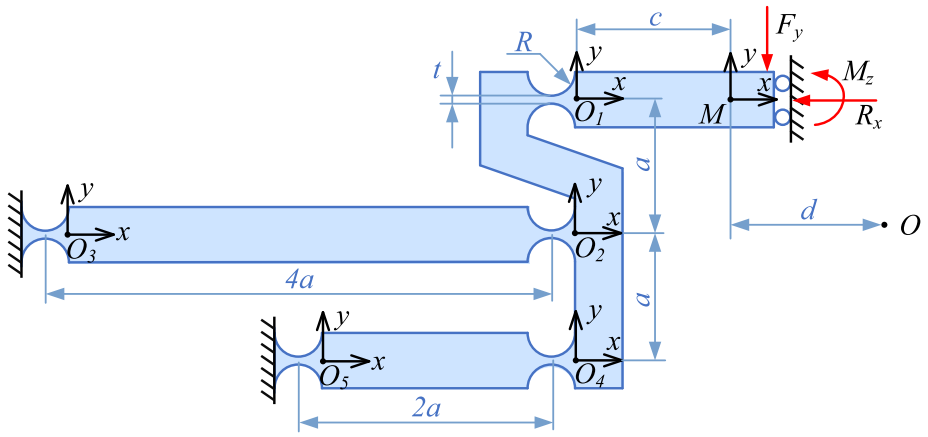

Fig. 5. Coordinate systems and parameters for a single FLGM.

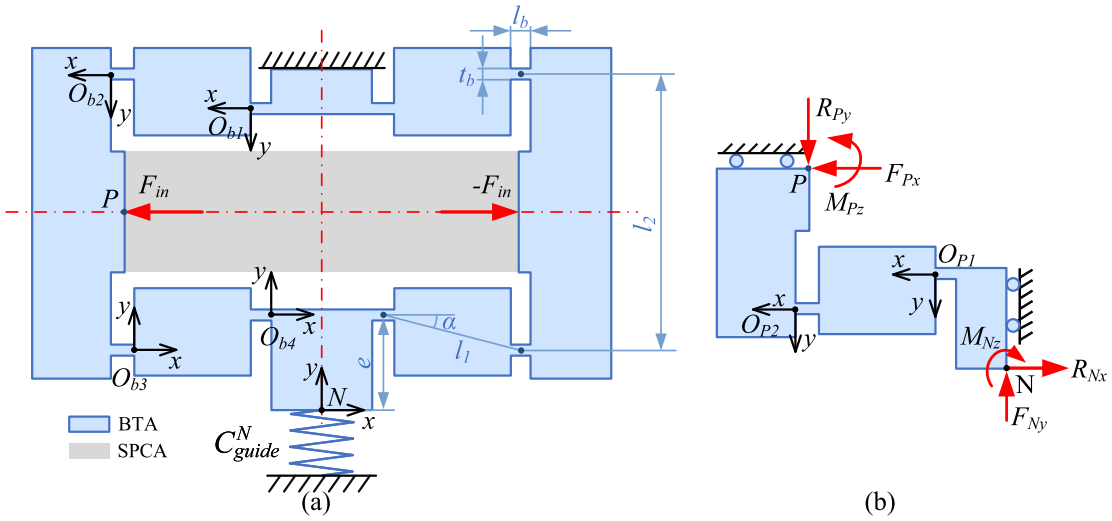

Fig. 6. Coordinate systems and parameters for BTA: (a) with respect to the output compliance, (b) with respect to the input compliance.

Flexure hinges O_2, O_3 and O_4, O_5 are serially connected respectively, then these two branches are connected in parallel. Subsequently, the parallel structure is serially connected to hinge O_1. Therefore, the equivalent compliance matrix of an FLGM with respect to endpoint M can be calculated as

$$C_g^M = \left[\left(C_{O2}^M + C_{O3}^M\right)^{-1} + \left(C_{O4}^M + C_{O5}^M\right)^{-1}\right]^{-1} + C_{O1}^M. \tag{12}$$

As is illustrated in Fig. 4(b), the compliance matrix of the left part of the linear guide consisting of two FLGMs with respect to center O is taken as:

$$C_{g\_left}^O = \left[\left(T_{M1}^O C_g^{M1} \left(T_{M1}^O\right)^T\right)^{-1} + \left(T_{M2}^O C_g^{M2} \left(T_{M2}^O\right)^T\right)^{-1}\right]^{-1} \tag{13}$$

where T_{M1}^O, T_{M2}^O denote the translation matrix from the coordinate system xyM_1, xyM_2 to xyO.

Due to the left–right symmetry of the linear guide, its compliance at point O can be obtained by:

$$C_{guide}^O = \left[\left(C_{g\_left}^O\right)^{-1} + \left(R(y,\pi) C_{g\_left}^O R(y,\pi)^T\right)^{-1}\right]^{-1} \tag{14}$$

where $R(y,\pi)$ is the rotation matrix from the left to the right section calculated by (9).

As for the forward BTA, output compliance and input compliance will be derived respectively. Firstly, coordinate systems and structural parameters with respect to the output compliance are depicted in Fig. 6(a). The global coordinate is attached to point N. The calculation procedures are similar to the analytical static modeling of the guiding module aforementioned. The compliance of the left part of the BTA will be first investigated. C_{bi} $(i = 1, \ldots, 4)$ represents the compliant matrix of the prismatic flexure beams in their local coordinates. The output compliance of the left part $C_{BTA\_left}^N$ can be calculated according to the serial structure as:

$$C_{BTA\_left}^N = \sum_{i=1}^{4} T_{bi}^N C_{bi} \left(T_{bi}^N\right)^T. \tag{15}$$

Then the compliance of the whole BTA at point N can be derived as:

$$C_{BTA}^N = \left[\left(C_{B\_left}^N\right)^{-1} + \left(R(y,\pi) C_{B\_left}^N R(y,\pi)^T\right)^{-1}\right]^{-1}. \tag{16}$$

The BTA and the linear guide are connected in parallel as shown in Fig. 4(c), hence the compliance matrix of the whole stage at the central point O is finally derived as:

$$C_{stage}^O = \left[\left(C_{guide}^O\right)^{-1} + \left(T_A^O C_{BTA}^N \left(T_A^O\right)^T\right)^{-1}\right]^{-1}. \tag{17}$$

Therefore, the output stiffness of the positioning stage is:

$$k_{out} = \left(C_{stage}^O(2,2)\right)^{-1}. \tag{18}$$

Secondly, when considering the input stiffness, only one-quarter of the BTA is analyzed as can be seen in Fig. 6(b). F_{Px} denotes the input force from the actuator and F_{Ny} represents the load force applied by the

linear guide. Assuming that the output end N is fixed, the compliance of left-down structure at the input point P can be calculated as:

$$C^P = T_{P1}^P C_{P1} \left(T_{P1}^P\right)^T + T_{P2}^P C_{P2} \left(T_{P2}^P\right)^T. \tag{19}$$

Then, combined with static equilibrium conditions, the linear and angular deflections at the input point P can be generated as the following equations:

$$\begin{cases} u_{Px} = C^P(1,1)F_{Px} + C^P(1,2)F_{Ny} + C^P(1,3)M_{Pz} \\ u_{Py} = C^P(2,1)F_{Px} + C^P(2,2)F_{Ny} + C^P(2,3)M_{Pz} \\ 0 = C^P(3,1)F_{Px} + C^P(3,2)F_{Ny} + C^P(3,3)M_{Pz}. \end{cases} \tag{20}$$

Moreover, the relationship between the load and deflection along y axis at point N can be generated from the linear guide:

$$\begin{cases} C_{guide}^N = T_O^N C_{guide}^O \left(T_O^N\right)^T \\ 2 \cdot u_{Py} + C_{guide}^N(2,2) \cdot 2F_{Ny} = 0. \end{cases} \tag{21}$$

In addition, let u_{in}, F_{in} denote the elongation and actuating force of the SPCA. For the whole BTA, there are the following relationships:

$$\begin{cases} u_{in} = 2 \cdot u_{Px} \\ F_{in} = 2 \cdot F_{Px}. \end{cases} \tag{22}$$

Finally, recall (20) and (21), the input compliance of the stage can be obtained as:

$$\begin{aligned} c_{in} = \frac{u_{in}}{F_{in}} = \frac{u_{Px}}{F_{Px}} &= C^P(1,1) - \frac{C^P(1,3)C^P(3,1)}{C^P(3,3)} \\ &+ \left(C^P(1,2) - \frac{C^P(1,3)C^P(3,2)}{C^P(3,3)}\right) \\ &\times \frac{C^P(2,1)C^P(3,3) - C^P(2,3)C^P(3,1)}{C^P(2,3)C^P(3,2) - C^P(2,2)C^P(3,3) - C^P(3,3)C_{guide}^N(2,2)} \end{aligned} \tag{23}$$

from which the input stiffness $k_{in} = 1/c_{in}$ can be derived.

Accordingly, the amplification ratio of this whole stage can be derived by:

$$\begin{aligned} A_s = \frac{2u_{Py}}{u_{in}} = \frac{u_{Py}}{u_{Px}} \\ = \frac{C_{guide}^A(2,2) \cdot \left(C^P(2,3)C^P(3,1) - C^P(2,1)C^P(3,3)\right)}{c_{in}\left(C^P(2,3)C^P(3,2) - C^P(2,3)C^P(3,3) - C^P(3,3)C_{guide}^A(2,2)\right)}. \end{aligned} \tag{24}$$

3.3. Dynamic modeling

Dynamic characteristics of CMs have attracted a lot of interest from researchers owing to their extended applications which demand high speeds and high frequencies. Theoretical calculation of the natural frequency is indispensable for future optimization and controllers' design. To describe the free vibration in the actuation direction of the guided stage, Lagrange's equation combined with PRBM and lumped mass method is utilized for dynamic modeling of the guided stage. The mass of flexure hinges is neglected because of their miniature sizes. Mass distribution is exhibited in Fig. 7. $m_i, T_i, J_i (i = 1, 2, \ldots, 6)$ represent the mass, kinetic energy, and rotational inertia of the rigid linkages in the compliant stage respectively. The generalized coordinate is selected as the input displacement u_{in}.

Combined with kinematic modeling conducted in Section 3.1, kinetic energy can be easily derived by the following equation:

$$T_i = \frac{1}{2}m_i v_i^2 + \frac{1}{2}J_i \dot{\theta}_i^2 \tag{25}$$

where v_i and θ_i denote the velocity and rotation angle of the ith rigid rod at the mass center.

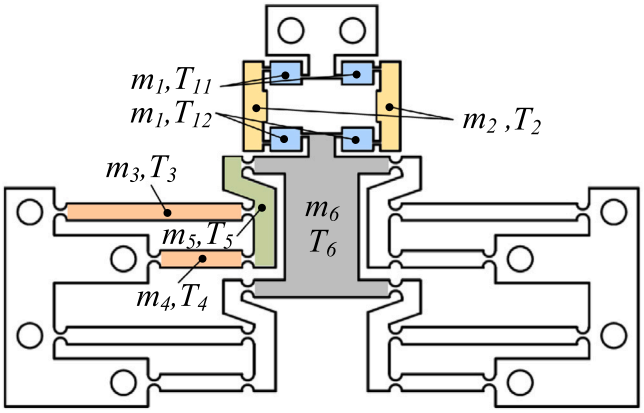

Fig. 7. Dynamic model scheme of the positioning stage with linear guide.

For the BTA, the kinetic energies can be derived as

$$\begin{cases} T_{11} = \frac{1}{2}m_1 \cdot v_{11}{}^2 + \frac{1}{2}J_1 \cdot \dot{\theta}_1{}^2 = \frac{1}{24}m_1 A_s{}^2 \dot{u_{in}}{}^2 \\ T_{12} = \frac{1}{2}m_1 \cdot v_{12}{}^2 + \frac{1}{2}J_1 \cdot \dot{\theta}_1{}^2 = \frac{1}{96}m_1\left(3 + A_s{}^2\right)\dot{u_{in}}{}^2 \\ T_2 = \frac{1}{2}m_2 v_2{}^2 = \frac{1}{8}m_2 A_s{}^2 \dot{u_{in}}{}^2 \\ T_{BTA} = 2\left(T_{11} + T_{12} + T_2\right). \end{cases} \tag{26}$$

For the FLGM, the kinetic energy can be deduced as:

$$\begin{cases} T_3 = \frac{1}{2}m_3 \cdot v_3{}^2 + \frac{1}{2}J_3 \cdot \dot{\theta}_3{}^2 = \frac{1}{6}m_3 A_s{}^2 \dot{u_{in}}{}^2 \\ T_4 = \frac{1}{2}m_4 \cdot v_4{}^2 + \frac{1}{2}J_4 \cdot \dot{\theta}_4{}^2 = \frac{1}{6}m_4 A_s{}^2 \dot{u_{in}}{}^2 \\ T_5 = \frac{1}{2}m_5 \cdot v_5{}^2 = \frac{1}{2}m_5 A_s{}^2 \dot{u_{in}}{}^2 \\ T_{guide} = 4\left(T_3 + T_4 + T_5\right). \end{cases} \tag{27}$$

For the central stage, the kinetic energy is:

$$T_6 = \frac{1}{2}m_6 \cdot v_6{}^2 = \frac{1}{2}m_6 A_s{}^2 \dot{u_{in}}{}^2. \tag{28}$$

As a result, the kinetic energy of the entire compliant stage is derived by:

$$\begin{aligned} T &= T_{BTA} + T_{guide} + T_6 \\ &= \frac{1}{16}m_1 \dot{u_{in}}{}^2 + \left(\frac{5}{48}m_1 + \frac{1}{4}m_2 + \frac{2}{3}m_3 + \frac{2}{3}m_4 + 2m_5 + \frac{1}{2}m_6\right) A_s{}^2 \dot{u_{in}}{}^2. \end{aligned} \tag{29}$$

Based on the virtual work principle, the potential energy of the mechanism can be obtained as:

$$V = \frac{1}{2}k_{in} u_{in}{}^2. \tag{30}$$

Substituting the total kinetic energy (29) and total potential energy (30) into Lagrange's equation:

$$\frac{d}{dt}\left(\frac{\partial T}{\partial \dot{u_{in}}}\right) - \frac{\partial T}{\partial u_{in}} + \frac{\partial V}{\partial u_{in}} = F \tag{31}$$

where $F = 0$ under free vibration circumstances. Thus the dynamic equation describing a free motion of the stage is derived as:

$$m_e \ddot{u_{in}} + k_{in} u_{in} = 0 \tag{32}$$

where m_e represents the equivalent mass and can be obtained by:

$$\begin{aligned} m_e &= \frac{\partial T}{\partial \dot{u_{in}}}\frac{1}{\dot{u_{in}}} = \frac{\partial T}{\partial \dot{u_{in}}} \cdot \frac{1}{\dot{u_{in}}} \\ &= \frac{1}{8}m_1 + \left(\frac{5}{24}m_1 + \frac{1}{2}m_2 + \frac{4}{3}m_3 + \frac{4}{3}m_4 + 4m_5 + m_6\right) A_s{}^2. \end{aligned} \tag{33}$$

Table 1
Design parameters for the guided stage.

Parameter	Value	Parameter	Value	Parameter	Value	Parameter	Value
t	0.7 mm	R	1 mm	t_b	0.5 mm	l_b	1.2 mm
α	11°	l_1	6.3 mm	l_2	12 mm	a	7.6 mm
c	6 mm	d	6 mm	e	6.35 mm	w	10 mm

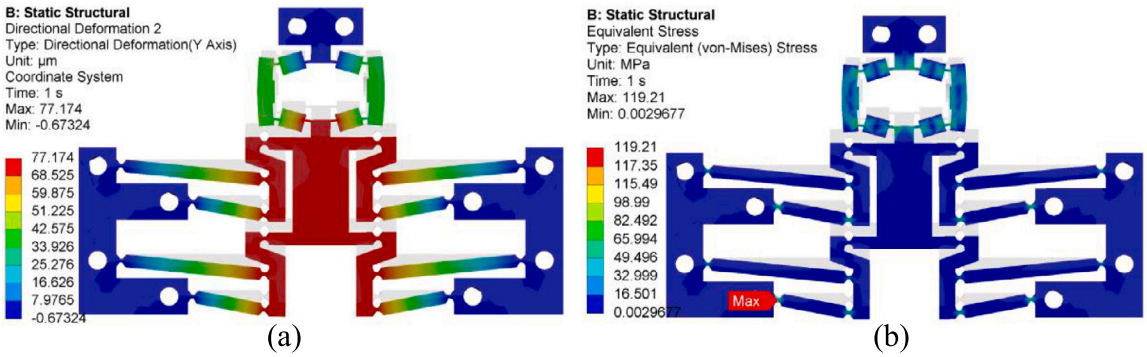

Fig. 8. Results of static FEA with an input displacement of 20 μm: (a) directional deformation in actuation direction, (b) von-Mises equivalent stress.

Finally, the natural frequency of the guided stage can be described as:

$$f = \frac{1}{2\pi}\sqrt{\frac{k_{in}}{m_e}} \tag{34}$$

where the input stiffness k_{in} is the inverse value of the input compliance calculated by (23).

4. Finite element analysis

To verify the results calculated by theoretical modeling, FEA is conducted via ANSYS Workbench software. The main design parameters of the stage are listed in Table 1 where w denotes the out-of-plane thickness. The material of the mechanism is chosen as aluminum alloy (AL7075-T6) and its physical parameters are Density = 2810 kg/m^3, Young's modulus = 71.7 GPa, Poisson's ratio = 0.33, and Yield strength = 503 MPa.

4.1. Kinematic and static simulation

Through static FEA, directional deformation behavior and von-Mises equivalent stress of the stage are acquired with a total input displacement u_{in} of 20 μm, as depicted in Fig. 8(a) and (b). The static simulation shows that the output displacement of the stage along the guiding direction and lateral direction are 77.162 μm and 0.415 μm, which indicates an excellent guiding ability with 0.54% cross-axis displacement rate. The slight parasitic motion is probably caused by the inhomogeneous mesh deducing from the unilateral preload screw hole on the BTA and the numerical calculation error. Meanwhile, the simulated amplification ratio can be obtained as 3.858. The simulated maximum equivalent stress is 119.21 MPa, which occurs at the flexure hinge with maximal rotation angle, meeting the material's strength condition.

Output displacements of the forward BTA and the guided stage concerning a series of input displacements ranging from 2 to 20 μm are also simulated by static FEA. The simulated results and the analytical results calculated by Eqs. (1) and (24) are plotted in Fig. 9. It can be observed that the amplification ratios given by the analytical modeling overestimate the simulation amplification ratios. And the compliance matrix method possesses a much higher kinematic and static modeling accuracy than the PRBM with respect to the amplification ratio. The discrepancies are probably caused by the practical deformation that exists in the rods considered rigid in the analytical modeling process.

Table 2
Kinematic, static, and dynamic performances of the guided stage.

Performance	k_{out} (N/μm)	k_{in} (N/μm)	A_s	f_1 (Hz)
Analytical	1.288	13.618	3.991	961.4
FEA	1.327	14.197	3.858	1171.1
Deviation[a] (%)	2.94	4.08	3.45	17.9
Experiments	/	/	3.792	856.9

[a] Deviation between analytical values and FEA values.

Table 3
Simulation results of the first-six order natural frequencies of the guided stage.

Mode	1	2	3	4	5	6
Frequency (Hz)	1173.1	2706.6	2865.1	3284.1	3657.9	5474.6

In addition, to acquire the output stiffness and input stiffness of the stage, constant forces of 100 N are loaded at the output end and input end, respectively. Then the results are calculated as 1.327 N/μm, 14.197 N/μm. The deviation of kinematic and static analytical results regarding the simulation is all within 4.08%, indicating the veracity of the aforementioned theoretical modeling. The results are tabulated in Table 2.

4.2. Dynamic simulation

Modal simulation is performed to validate the feasibility of the design. The simulated first four modal shapes are shown in Fig. 10 and first-six order resonant frequencies are listed in Table 3. The first modal shape is the translation along the guiding axis with a natural frequency of 1173.1 Hz, which is higher than the analytical result. It is probably caused by the influence of the condition and meshing setting of the FEA. It can be observed that the second-order natural frequency is more than twice of the first mode, which verifies that the stage has one degree of freedom and ideal dynamic characteristics.

5. Experimental verification

5.1. Experimental setup

The prototype of the proposed guided stage has been fabricated using AL7075-T6 by the wire electrical discharge machining (WEDM) as shown in Fig. 11(a). The schematic diagram of the experiment system is shown in Fig. 12 where Simulink Real-Time is employed.

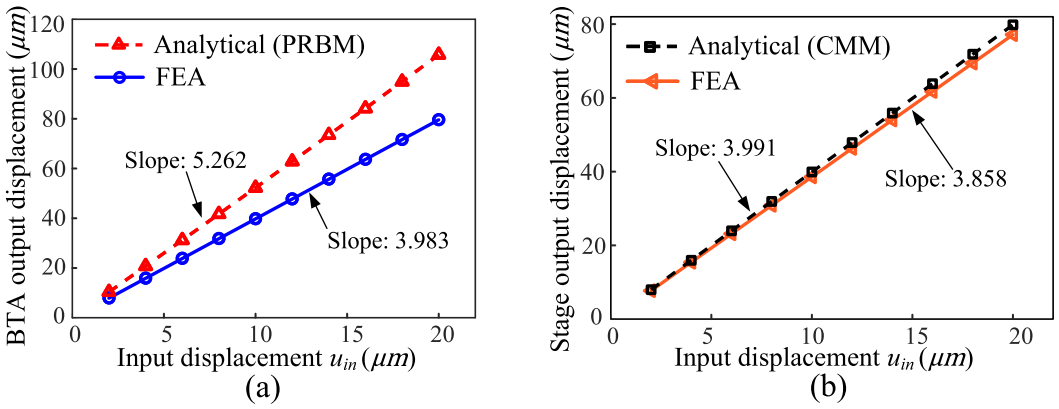

Fig. 9. Comparison of simulation and analytical results of output displacements of (a) solitary BTA module and (b) whole guided positioning stage.

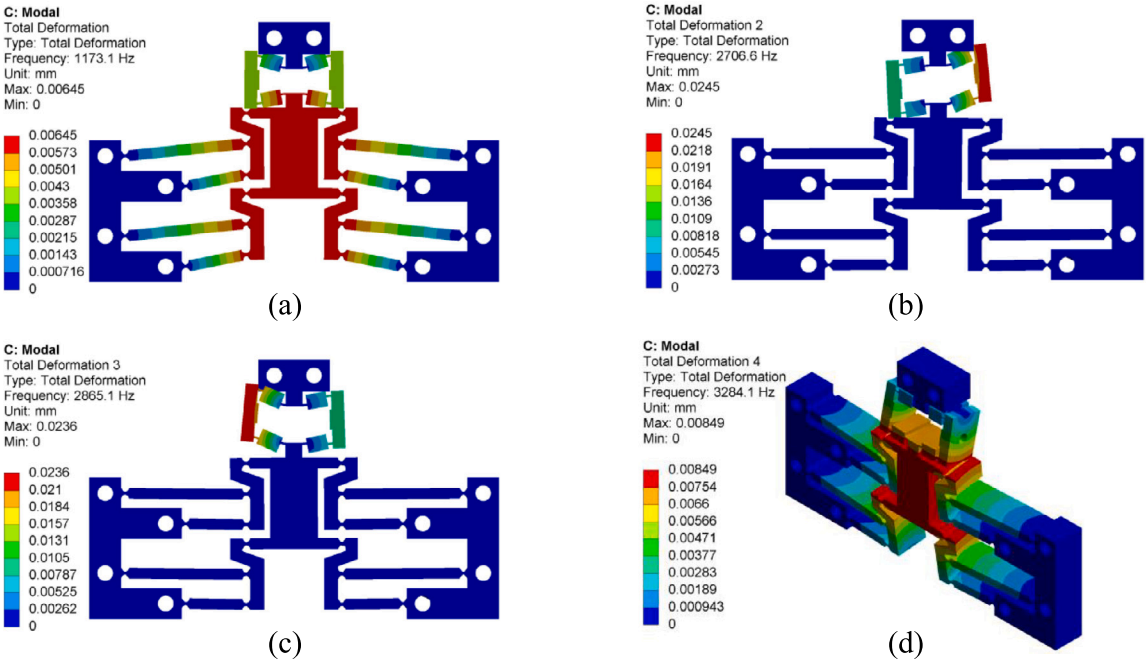

Fig. 10. First four modal shapes of the stage simulated by modal FEA: (a) first mode, (b) second mode, (c) third mode, (d) fourth mode.

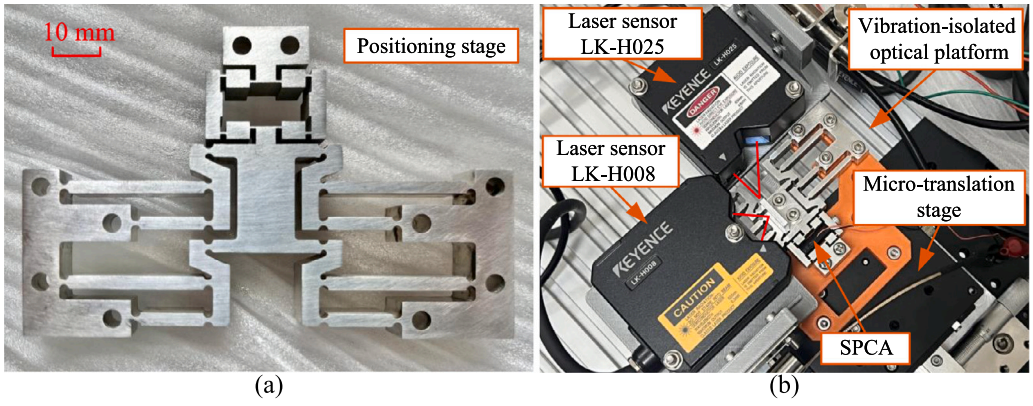

Fig. 11. Prototype of the proposed guided stage. (a) Guided stage fabricated by WEDM, (b) Experiment setup.

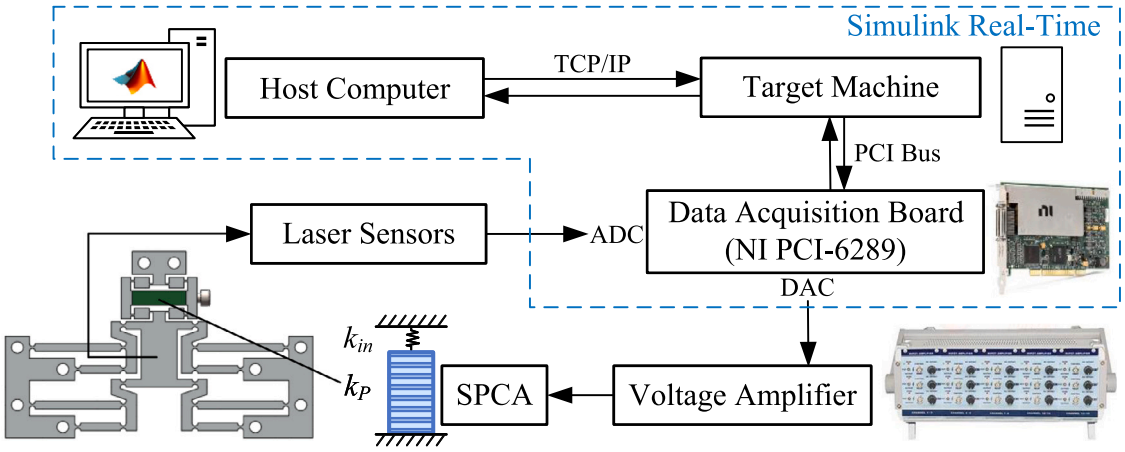

Fig. 12. Schematic diagram of the experiment system.

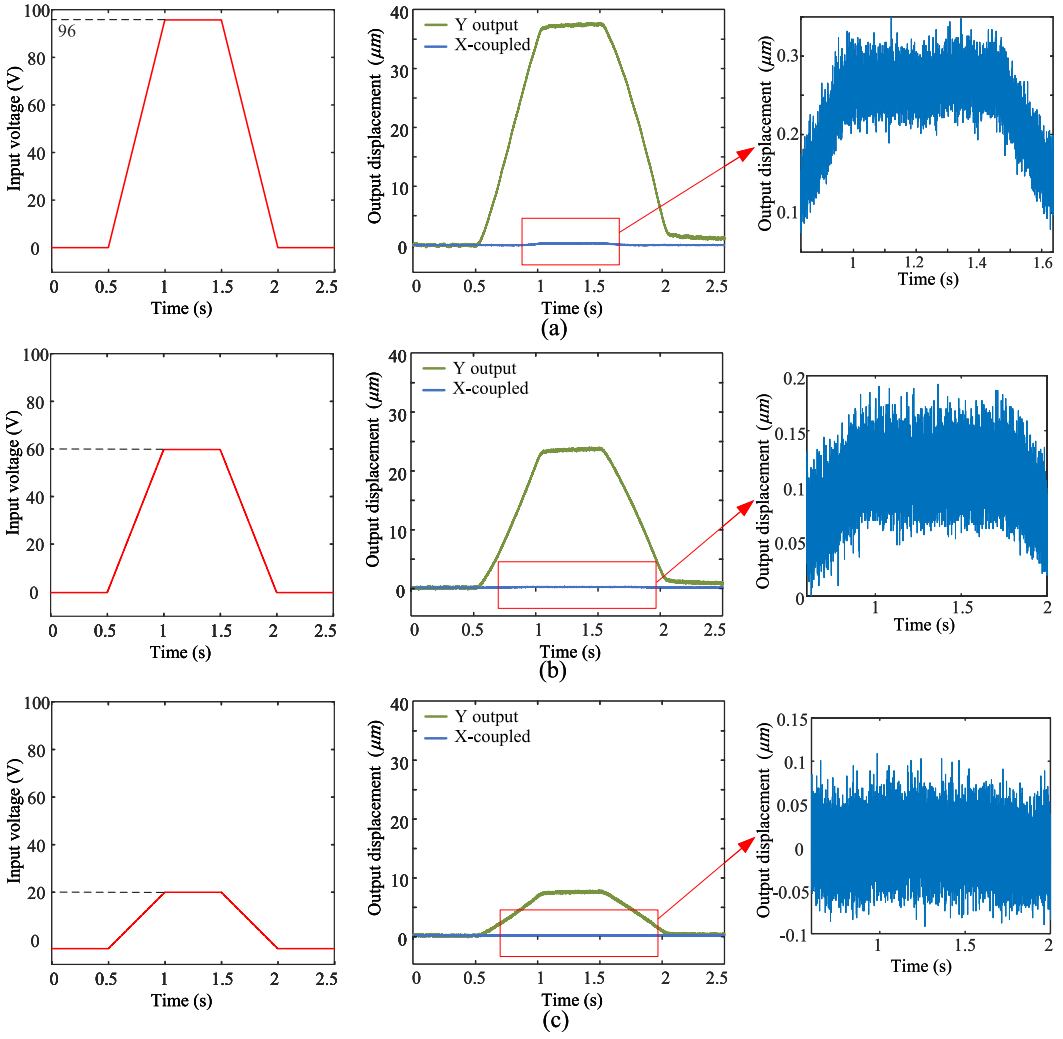

Fig. 13. Experimental results of experimental displacement test: (a) input trapezoidal signal, (b) output displacements of the guided stage, (c) lateral coupled displacement.

The host computer and target machine are connected by a network cable. The compliant guided stage is inserted with a piezoelectric stack (PSt 150/5 × 5/20H from COREMORROW, Inc.) which can generate a nominal displacement of 20 μm under 150 V input voltage. The output displacements along guiding and lateral direction are synchronously measured by two different laser sensors LK-H025 (Keyence) and LK-H008 (Keyence), respectively. The orthogonal arrangement of sensors is illustrated in Fig. 11(b). LK-H025 has a measurement range of ±3 mm and a repeatability of 20 nm, while LK-H008 has a measurement range of ±0.5 mm and a repeatability of 5 nm. A signal generator

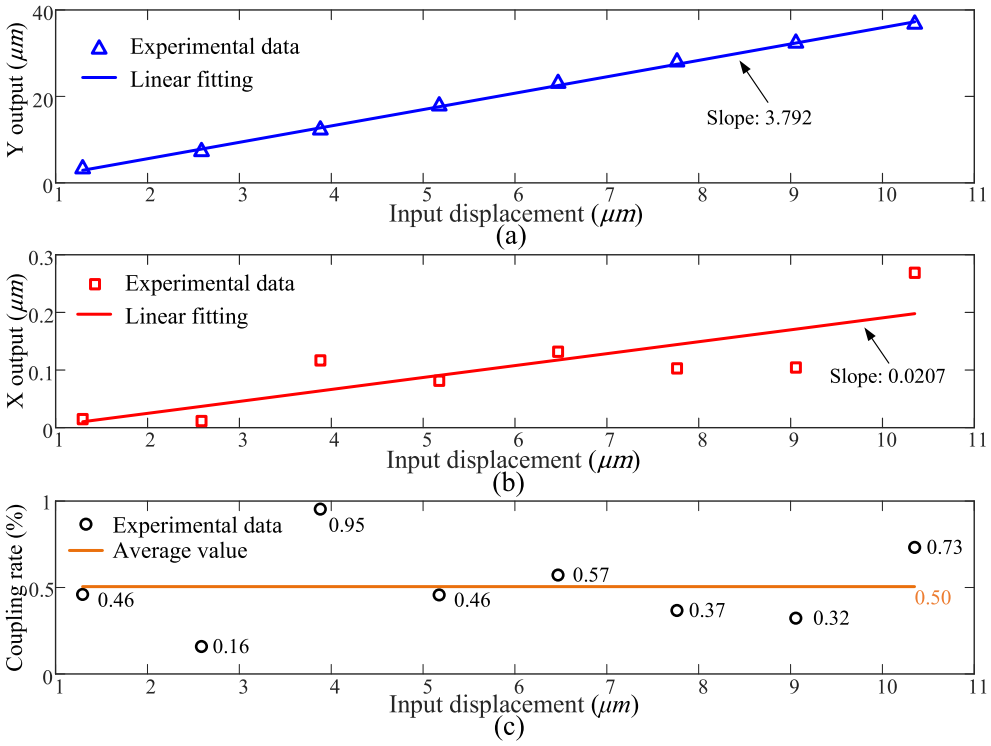

Fig. 14. Experimental results of output–input displacement steady-state test (open control): (a) output displacement in guiding direction, (b) lateral coupled output displacement, (c) displacement coupling rate.

(DAQ PCI-6289 from National Instrument) is installed on the target machine via PCI bus to generate 0–10 V control signals and to read out data from the laser sensors. A power amplification module (E03.00 from COREMORROW, Inc.) with a voltage amplification ratio of 12 is utilized to magnify the control voltage and actuate the SPCA.

5.2. Experimental tests

Experimental tests are conducted to verify the properties of the designed guided stage. Firstly, a series of trapezoidal voltage signals with different maximum voltages are applied to the piezoelectric actuator as plotted in Fig. 13. The input trapezoidal signals and results from laser sensors are recorded. For example, when the maximum input voltage is set as 96 V as shown in Fig. 13(a), it can be observed that the output displacements of the guided stage along the guiding direction and lateral direction are 37.261 μm and 0.272 μm respectively. The corresponding input displacement is about 10.35 μm under the influence of stiffness coupling of the compliant stage and the SPCA. Hence the displacement amplification ratio and coupling rate can be calculated as 3.60 and 0.73% in this circumstance. From these steady-state experimental results, the displacement amplification ratio of the fabricated prototype can be further investigated. The relationship between the output and input displacement is illustrated in Fig. 14. A linear fitting relation of the output–input characteristic in the guiding direction is obtained with a slope of 3.792, which can be deemed as the experimental displacement amplification ratio of the stage. And the observed average cross-axis coupling rate is 0.50%, which confirms the guiding property.

Secondly, a 1 Hz sine-wave signal with incremental amplitude is input to the SPCA, as shown in Fig. 15(a). The displacement tracking results and the hysteresis curve are obtained and depicted in Fig. 15(b), (c), and (d). Due to the intrinsic nonlinearity and creep properties of the piezoelectric actuators, the hysteresis of the stage exists under an open-loop system. The maximum displacements of the guiding axis and coupled axis are 101.3 μm and 0.35 μm, which indicate a dynamic cross-coupling rate of around 0.35%. Finally, a sine-swept signal with a peak-peak amplitude of 12 V and a frequency increasing from 10 to 1200 Hz is exerted on the SPCA. It is found that the first-order natural frequency of the prototype is 856.9 Hz, which is smaller than both analytical and simulation results and close to the analytical results.

5.3. Performance evaluation and discussion

Overall, the experimental results validate the veracity and efficacy of the theoretical modeling and the proposed guided stage. It can be observed that the natural frequency calculated by FEA overestimates the theoretical and experimental result, which is probably caused by the impact of the actuator and its preloading bolt that is overlooked in FEA simulation. Moreover, the discrepancy between the experimental and simulated amplification ratio may arise from manufacturing tolerance and measurement errors. In addition, to improve the repeatability and positioning precision of the proposed stage, a closed-loop control strategy can be designed and applied in the future.

The performances of the proposed stage and previous advanced studies on compliant guided stages are compared in Table 4. The results show that the proposed guided stage exhibits a moderate amplification ratio and travel range. An adequate cross-axis coupling rate which proves the good guiding ability of the proposed mechanism is verified. Moreover, the proposed stage possesses a high first-order natural frequency which is significant for the dynamic characteristics and high-speed applications. Also, the proposed FLGM can be easily combined with other types of actuators and displacement amplifiers to achieve precision positioning for multifarious applications.

6. Conclusions

This paper proposes a novel design of a piezo-actuated compliant positioning stage composed of a forward bridge-type displacement amplifier and a linear guiding mechanism. A novel F-shaped straight-line mechanism with a simple and compact structure is devised and utilized

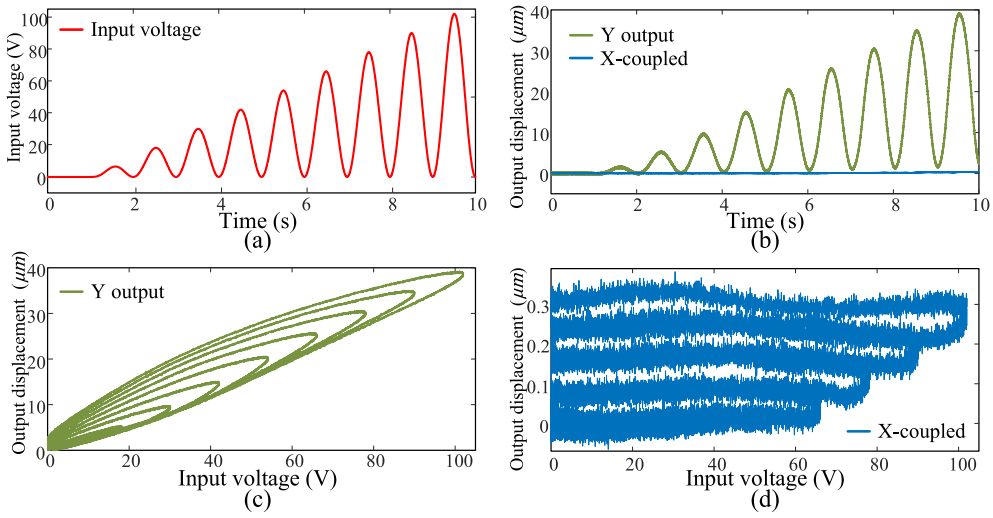

Fig. 15. Experimental results of hysteresis test: (a) input sine-wave signal, (b) output displacement in guiding direction, (c) the hysteresis curve in guiding direction, (d) the hysteresis curve in coupled direction.

Table 4
Comparisons with previous studies.

Studies	D.o.F	f_1 (Hz)	Amplification ratio	Dimensions (mm^3)	Travel range (μm)	Coupling rate
[26]	2	18.6	1	244 × 244 × –	12400 & 12200	1.57% & 1.66%
[37]	2	570	5.2 & 5.4	165 × 145 × 18	31.5 & 31.5	1%
[18]	1	265.5	3.0001	90 × 150 × 10	51.9	–
[38]	2	483	5.14 & 5.36	142 × 142 × 10	40.2 & 42.9	0.58%
[9]	1	129.72	1	100 × 100 × 5	5580	0.31%
[39]	2	278.9	3.16	150 × 150 × 30	120 & 120	0.65%
This work	1	856.9	3.792	100 × 64 × 10	75.84	0.95%

in the linear guide to restrict parasitic motion and enhance positioning accuracy. The analytical kinematic modeling is conducted based on PRBM to certify the function of an FLGM to generate an approximate straight-line motion. Output stiffness, input stiffness, and amplification ratio of the guided stage are obtained through static modeling established by the compliance matrix method. First-order natural frequency is calculated via dynamic modeling derived from Lagrange's equation. Furthermore, FEA simulation studies are undertaken to evaluate the performances of the proposed stage. FEA results confirm the accuracy of the theoretical modeling with slight deviation. The compliant stage has been fabricated by WEDM and tested by experiments. The experimental results indicate that the guided stage exhibits an amplification ratio of 3.792, a cross-axis coupling rate below 0.95%, and a high natural frequency of 856.9 Hz. It is verified that the proposed mechanism can meet the requirements of reducing the parasitic motion thus demonstrating a new prototype of high precision linear guide. Future work may involve structural optimization and closed-loop precision control experiments for more applications.

CRediT authorship contribution statement

Yitong Li: Conceptualization, Methodology, Writing – review & editing, Writing – original draft. **Tingting Ye:** Methodology, Writing – original draft, Writing – review & editing. **Jie Ling:** Funding acquisition, Writing – review & editing. **Xiaohui Xiao:** Methodology, Writing – review & editing. **Zhao Feng:** Conceptualization, Funding acquisition, Supervision, Writing – original draft, Writing – review & editing.

Declaration of competing interest

The authors declare that they have no known competing financial interests or personal relationships that could have appeared to influence the work reported in this paper.

Acknowledgments

This work was supported by Knowledge Innovation Program of Wuhan-Shuguang Project, China (Grant No. 2023010201020252), Guangdong Basic and Applied Basic Research Foundation, China (Grant No. 2023A1515110156), and Natural Science Foundation of Jiangsu Province, China (Grant No. BK20210294).

References

[1] Chang Q, Gao X, Liu Y, Deng J, Zhang S, Chen W. Development of a cross-scale 6-DOF piezoelectric stage and its application in assisted puncture. Mech Syst Signal Process 2022;174:109072.
[2] Wang G, Xu Q. Design and precision position/force control of a Piezo-driven microinjection system. IEEE/ASME Trans Mechatronics 2017;22(4):1744–54.
[3] Ding B, Yang Z-X, Zhang G, Xiao X. Optimum design and analysis of flexure-based mechanism for non-circular diamond turning operation. Adv Mech Eng 2017;9(12):1687814017743353.
[4] Yuan L, Wang L, Qi R, Zhao Z, Jin J, Zhao C. A novel hollow-type XY piezoelectric positioning platform. Int J Mech Sci 2023;255:108496.
[5] Yang X, Zhu W-L, Zhu Z, Zhu L-M. Design, assessment, and trajectory control of a novel decoupled robotic nanomanipulator. IEEE/ASME Trans Mechatronics 2022;27(5):3999–4010.
[6] Ling M, Howell LL, Cao J, Chen G. Kinetostatic and dynamic modeling of flexure-based compliant mechanisms: A survey. Appl Mech Rev 2020;72(3):030802.
[7] Zhu J, Hao G, Liu T, Li H. Design of an over-constraint based nearly-constant amplification ratio compliant mechanism. Mech Mach Theory 2023;186:105347.
[8] Ling M, Zhang C, Chen L. Optimized design of a compact multi-stage displacement amplification mechanism with enhanced efficiency. Precis Eng 2022;77:77–89.
[9] Lyu Z, Xu Q, Zhu L. Design of a compliant vertical micropositioning stage based on lamina emergent mechanisms. IEEE/ASME Trans Mechatronics 2023;28(4):2131–41.
[10] Li R, Yang Z, Cai B, Chen G, Wu B, Wei Y. A compliant guiding mechanism utilizing orthogonally oriented flexures with enhanced stiffness in degrees-of-constraint. Mech Mach Theory 2022;167:104555.
[11] Liu T, Hao G. Design of a cylindrical compliant linear guide with decoupling parallelogram mechanisms. Micromachines 2022;13(8).

[12] Wang F, Huo Z, Liang C, Shi B, Tian Y, Zhao X, Zhang D. A novel actuator-internal micro/nano positioning stage with an arch-shape bridge-type amplifier. IEEE Trans Ind Electron 2019;66(12):9161–72.
[13] Hao G, Yu J. Design, modelling and analysis of a completely-decoupled XY compliant parallel manipulator. Mech Mach Theory 2016;102:179–95.
[14] Sun Y, Lueth TC. Safe manipulation in robotic surgery using compliant constant-force mechanism. IEEE Trans Med Robot Bionics 2023;5(3):486–95.
[15] Ling J, Ye T, Feng Z, Zhu Y, Li Y, Xiao X. A survey on synthesis of compliant constant force/torque mechanisms. Mech Mach Theory 2022;176:104970.
[16] Ye T, Ling J, Yao T, Xiao X. Design of a 2-DOF constant force compliant microgripper for optical switch assembly. In: IECON 2020 the 46th annual conference of the IEEE industrial electronics society. 2020, p. 4403–8.
[17] Tang H, Li Y. Design, analysis, and test of a novel 2-DOF nanopositioning system driven by dual mode. IEEE Trans Robot 2013;29(3):650–62.
[18] Nguyen V-K, Pham H-T, Pham H-H, Dang Q-K. Optimization design of a compliant linear guide for high-precision feed drive mechanisms. Mech Mach Theory 2021;165:104442.
[19] Zhao D, Zhu Z, Huang P, Guo P, Zhu L, Zhu Z. Development of a piezoelectrically actuated dual-stage fast tool servo. Mech Syst Signal Process 2020;144:106873.
[20] Lyu Z, Xu Q. Design and testing of a large-workspace XY compliant manipulator based on triple-stage parallelogram flexure. Mech Mach Theory 2023;184:105287.
[21] Gräser P, Linß S, Harfensteller F, Torres M, Zentner L, Theska R. High-precision and large-stroke XY micropositioning stage based on serially arranged compliant mechanisms with flexure hinges. Precis Eng 2021;72:469–79.
[22] Zhao H, Bi S, Yu J. A novel compliant linear-motion mechanism based on parasitic motion compensation. Mech Mach Theory 2012;50:15–28.
[23] Hricko J. Design of compliant micro-stage based on Peaucellier-Lipkin straight-line mechanism. In: 2014 23rd international conference on robotics in alpe-adria-danube region. RAAD, 2014, p. 1–6.
[24] Beroz J, Awtar S, Bedewy M, Tawfick S, Hart AJ. Compliant microgripper with parallel straight-line jaw trajectory for nanostructure manipulation. In: Proceedings of 26th American society of precision engineering annual meeting, denver, CO. 2011.
[25] Chen W, Shi X, Chen W, Zhang J. A two degree of freedom micro-gripper with grasping and rotating functions for optical fibers assembling. Rev Sci Instrum 2013;84(11):115111.
[26] Wan S, Xu Q. Design and analysis of a new compliant XY micropositioning stage based on roberts mechanism. Mech Mach Theory 2016;95:125–39.
[27] Wang L, Chen W, Liu J, Deng J, Liu Y. A review of recent studies on non-resonant piezoelectric actuators. Mech Syst Signal Process 2019;133:106254.
[28] Al-Jodah A, Shirinzadeh B, Ghafarian M, Das TK, Pinskier J, Tian Y, Zhang D. Modeling and a cross-coupling compensation control methodology of a large range 3-DOF micropositioner with low parasitic motions. Mech Mach Theory 2021;162:104334.
[29] Wang X, Meng Y, Huang W-W, Li L, Zhu Z, Zhu L. Design, modeling, and test of a normal-stressed electromagnetic actuated compliant nano-positioning stage. Mech Syst Signal Process 2023;185:109753.
[30] Howell LL, Magleby SP, Olsen BM. Handbook of compliant mechanisms. John Wiley & Sons; 2013.
[31] Xu Q, Li Y. Analytical modeling, optimization and testing of a compound bridge-type compliant displacement amplifier. Mech Mach Theory 2011;46(2):183–200.
[32] Ling M, Cao J, Zeng M, Lin J, Inman DJ. Enhanced mathematical modeling of the displacement amplification ratio for piezoelectric compliant mechanisms. Smart Mater Struct 2016;25(7).
[33] Cao J, Ling M, Inman DJ, Lin J. Generalized constitutive equations for piezo-actuated compliant mechanism. Smart Mater Struct 2016;25(9):095005.
[34] Lobontiu N, Paine JS, Garcia E, Goldfarb M. Design of symmetric conic-section flexure hinges based on closed-form compliance equations. Mech Mach Theory 2002;37(5):477–98.
[35] Ru C, Liu X, Sun Y, et al. Nanopositioning technologies. Fundam Appl 2016.
[36] Chen G, Liu X, Du Y. Elliptical-arc-fillet flexure hinges: Toward a generalized model for commonly used flexure hinges. J Mech Des 2011;133(8):081002.
[37] Zhu W-L, Zhu Z, Guo P, Ju B-F. A novel hybrid actuation mechanism based XY nanopositioning stage with totally decoupled kinematics. Mech Syst Signal Process 2018;99:747–59.
[38] Wang F, Zhao X, Huo Z, Shi B, Liang C, Tian Y, Zhang D. A 2-DOF nanopositioning scanner with novel compound decoupling-guiding mechanism. Mech Mach Theory 2021;155:104066.
[39] Lee H-J, Woo S, Park J, Jeong J-H, Kim M, Ryu J, Gweon D-G, Choi Y-M. Compact compliant parallel XY nano-positioning stage with high dynamic performance, small crosstalk, and small yaw motion. Microsyst Technol 2018;24(6):2653–62.